RSC Advances

PAPER

View Article Online
View Journal | View Issue

Cite this: *RSC Adv.*, 2017, **7**, 1956

Preparation and properties of a novel graphene fluoroxide/polyimide nanocomposite film with a low dielectric constant

Xiao Chen, Haohao Huang,* Xia Shu, Shumei Liu and Jianqing Zhao*

Received 17th October 2016
Accepted 25th November 2016

DOI: 10.1039/c6ra25343a

www.rsc.org/advances

This paper introduces an effective approach to fabricate novel graphene/polyimide nanocomposite films with a low dielectric constant. Graphene fluoroxide (GFO) nanosheets were produced through the exfoliation of graphite fluoroxide (GiFO) in *N*-methyl-2-pyrrolidone (NMP). GFO nanosheets reacted with 4,4′-diaminodiphenyl ether (ODA) to become ODA-functioned GFO (GFO-ODA) with amine end groups, which provided reactive sites for covalent bonding with PI chains. GFO-ODA/PI composite films were prepared *via* the thermal imidization of a GFO-ODA/PAA solution. In this composite, GFO-ODA nanosheets were chemically bonded to the PI matrix. The dielectric constant of the films depended on the loading of GFO-ODA and its minimum value reached 2.75 (at 10^6 Hz) when the content of GFO-ODA was 1.0 wt%. Strong GFO-ODA nanosheets facilitate the load transfer and enhance the mechanical properties of PI films. GFO-ODA/PI film with 1.0 wt% loading had a Young's modulus ~40% larger than pure PI film. In addition, the incorporation of GFO-ODA increased the glass transition temperature of the films and had no significant effect on the thermal stability.

1. Introduction

Polyimide (PI), one of the high performance dielectric materials, has been used in microelectronics for interconnections and packaging, because of its excellent thermal stability, mechanical properties, and good chemical resistance, as well as relatively low dielectric constant (ε).[1–3] PI possesses a lower dielectric constant in the range of 3.4–3.7 than traditional dielectric materials, such as silica. However, with the rapid development of microelectronics, the dielectric constant of common PI is still too high to meet the requirement for ultra-large-scale integration multilevel interconnections.[2] The formation of intra- and inter-chain charge transfer complex in PI results in a relatively high dielectric constant for PI.[4] It is well known that the incorporation of fluorinated substituents into polymers can decrease the dielectric constant due to the high electronegativity of the fluorine atoms and the low polarizability of the C–F bond as well as the increase in free volume.[5–7] Nevertheless, the introduction of fluorinated groups into monomers usually decreases the activity of the diamine, resulting in poor mechanical properties of polyimide because of the low molecular weight.[5] Therefore, preparation of fluorinated PI with low dielectric constant and relatively high mechanical properties is still a great challenge.

In the past years, increasing scientific and industrial attention has been paid to the graphene-containing polymer composites because of their extraordinary physical and chemical properties. Graphene is a two-dimensional (2D) network of carbon atoms and has attracted intensive interest since its successful exfoliation from graphite.[8] Graphene is considered to be the strongest material ever measured due to its Young's modulus of ~1 TPa and strength of ~130 GPa.[9] Moreover, graphene has high thermal conductivity and charge carrier mobility, which are 5000 W m^{-1} K^{-1} and 0.25 × 10^6 cm^2 V^{-1} s^{-1}, respectively.[10,11] These properties, together with extremely high surface area and gas impermeability,[12] provide a great potential in fabricating high performance polymer composites for graphene.[13–15]

In order to improve the surface and dispersion properties of graphene, graphene was often modified to obtain graphene oxide (GO) or graphene fluoride (GF). Graphene oxide is considered to be more hydrophilic than graphene because of the oxygen-containing functional groups.[16–18] As a result, GO can be readily dispersed in polar solvents and matrix.[19,20] GF is an optical transparent semiconductor with a wide bandgap (~3 eV), relatively high Young's modulus (~0.3 TPa), and high-quality insulating property (>10^{12} Ω).[21–23] GF is well-known for its applications in lithium ion batteries,[21,24] lubricants,[25] thermoelectric devices,[26] and photoluminescence materials.[27] Recently, Ho *et al.*[28] investigated the dielectric constant of multilayer GF, which was found to be only ~1.2. Therefore, GF is expected to be an ideal nano-filler to decrease the dielectric constant of PI film. Recently, graphene fluoroxide (GFO),

College of Materials Science and Engineering, South China University of Technology, Guangzhou, 510640, China. E-mail: hhhuang@scut.edu.cn; psjqzhao@scut.edu.cn; Tel: +86-20-87110966

combining the properties of both GO and GF, has found applications in optical limiting applications,[29] amphiphobic coating,[30] primary lithium batteries,[31] and drug delivery.[32]

In the present paper, functioned GiFO was employed to fabricate a series of PI composite films. Graphite fluoride (GiF) as raw material was first oxidized to prepare graphite fluoroxide (GiFO) based on the process described in our previous work.[33] Then GFO was obtained by exfoliating GiFO and was modified with excess 4,4′-diaminodiphenyl ether (ODA). The amine-modified GFO nanosheets (GFO-ODA) provided a reactive platform for covalently bonding with PI chains. The dielectric, mechanical, and thermal properties of the GFO-ODA/PI films were examined at various GFO-ODA loadings. For the purpose of comparison, PI composite films with GF or GFO were also prepared.

2. Experimental

2.1. Materials

GiF powder with a fluorine content of 28.4 wt% was obtained from Alfa Aesar (China). Concentrated sulfuric acid (H_2SO_4), phosphorus pentoxide (P_2O_5), potassium permanganate ($KMnO_4$), sodium nitrate ($NaNO_3$), potassium persulfate ($K_2S_2O_8$), concentrated hydrochloric acid (HCl), 30% hydrogen peroxide (H_2O_2) solution, and ethanol were purchased from Guangzhou Chemical Reagent Factory (China). Above reagents were all of analytical grade and used as received. *N*-Methyl-2-pyrrolidone (NMP) was also purchased from Guangzhou Chemical Reagent Factory (China), and was left overnight in the presence of P_2O_5 and then distilled under reduced pressure before use. 4,4′-Diaminodiphenyl ether (ODA, 98%) was obtained from TCI Co., Ltd. (Japan) and was dried in vacuum at 60 °C for 24 h prior to use. Pyromellitic dianhydride (PMDA, 99%) was supplied by Aladdin Chemistry Co., Ltd. (China) and was dried in vacuum at 140 °C for 48 h prior to use.

2.2. Synthesis of GFO and GFO-ODA

Polyimide nanocomposite was prepared following the procedure illustrated in Scheme 1. First, GiFO nanosheets were synthesized from GiF powder with the routine as previously reported.[33] Typically, GiF powder (2 g) was added into a mixture of $K_2S_2O_8$ (1 g), P_2O_5 (1 g), and concentrated H_2SO_4 solution (15.2 mL). After stirring at 80 °C for 8 h, a resultant dark mixture was obtained. After being cooled to room temperature, the mixture was diluted with distilled water. The pre-oxidized product was washed with distilled water to remove any residual acid and dried overnight at 60 °C in an air oven. The pre-oxidized product was then subjected to oxidation *via* the modified Hummers method.[34]

The pre-oxidized product was added into the mixture of concentrated H_2SO_4 solution (54 mL) and $NaNO_3$ (1 g). After being cooled to 0–5 °C, the mixture was stirred for 15 min and $KMnO_4$ (6 g) was added in five batches, and then successively reacted at 0–5 °C for 4 h, at 35 °C for 2 h, and at 95 °C for 15 min. During the last stage, 80 mL distilled water was slowly added. The reaction was terminated by the addition of 400 mL distilled water and 10 mL 30% H_2O_2 solution. After being left overnight, a dark brown solid precipitated out of the solution, while a light grey phase floated on the dispersion surface. The precipitate was collected *via* centrifugation and washed with concentrated HCl solution and with distilled water repeatedly until the supernatant became neutral. The GiFO sample was obtained after being freeze dried.

To synthesize GFO-ODA nanosheets, GFO suspension was first obtained by exfoliating GiFO in NMP. Then 0.3 g ODA was added into 100 mL GFO suspension (1.0 mg mL^{-1}) and then stirred at 60 °C for 24 h in nitrogen atmosphere. To remove the excess ODA, the mixture was filtered and washed with NMP for a few times. The GFO-ODA sample was finally obtained after being dried in vacuum overnight.

2.3. Preparation of GFO-ODA/PI composite films

Typically, 0.0107 g GFO-ODA was dispersed in NMP by sonication for 2 h. To synthesize the PI-precursor (poly(amic acid), PAA), 1.0339 g of ODA (5.00 mmol) was put into a three-neck flask containing GFO-ODA suspension under nitrogen purge at room temperature. When ODA was completely dissolved, 1.1149 g of PMDA (5.05 mmol) was introduced to the flask in four batches. After being stirred overnight, a viscous GFO-ODA/PAA solution was obtained. This mixture was subsequently cast on glass dishes which had been cleaned with distilled water, and the sample was then thermal imidized sequentially at 80 °C for 1 h, 100 °C for 1 h, 200 °C for 1 h, and 300 °C for 2 h in a vacuum oven. Upon thermal imidization, a PI composite film containing 0.5 wt% GFO-ODA was obtained. The GFO-ODA/PI films with 1.0 wt% and 2.0 wt% of GFO-ODA were also prepared using the same procedure. For purpose of comparison, the PI films incorporated with GF or GFO nanosheets were also prepared *via* the same method.

2.4. Characterization

Fourier transform infrared spectra (FT-IR) from 400 to 4000 cm^{-1} were recorded by a VERTEX70 spectrometer (Bruker,

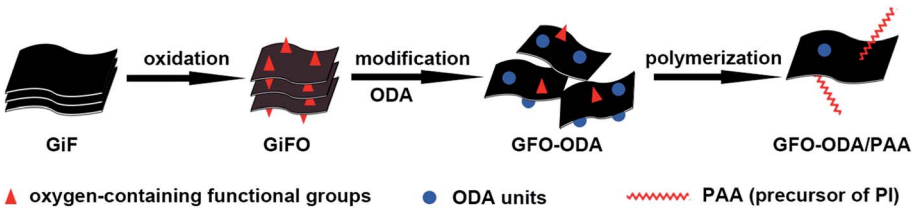

Scheme 1 Preparation procedure of GFO-ODA/PAA.

Germany). X-ray photoelectron spectroscopy (XPS) analysis was carried out on an Axis Ultra DLD X-ray photoelectron spectrometer (Kratos, UK) with Al K_α radiation ($h\nu = 1486.6$ eV). X-ray diffraction (XRD) measurements were performed on a D8 Advance X-ray diffractometer (Bruker, Germany) with Cu K_α radiation ($\lambda = 0.15418$ nm). Step scanning was used with 2θ intervals from 5° to 30°. Raman spectra were obtained on a LabRAM Aramis Micro-Raman spectrometer (HORIBA, France) using Helaser beam excitation ($\lambda = 632.8$ nm). Thermogravimetric analysis (TGA) was carried out on a TG209F1 instrument (NETZSCH, Germany) from 30 to 900 °C under nitrogen flow at a heating rate of 10 °C min^{-1}. To measure the modulus and tensile strength of PI composite films, samples were cut into sheets with a width of 10 mm, and were tested on a material testing system (Instron 5967, US) according to ASTM D882-12 standard. The speed of the crosshead was 5 mm min^{-1}. An average of at least five individual determinations was used. The thermal dynamic mechanical behavior and glass transition temperature (T_g) of PI composite films were carried out on dynamic mechanical analyzer (DMA, NETZSCH 242C, Germany). All the tests were run from 30 to 400 °C at a heating rate of 3 °C min^{-1} and a frequency of 1 Hz. The morphology of the fractured surfaces of PI composite films was observed on a scanning electron microscope (SEM, FEI Nova NonaSEM430, US) at an accelerating voltage of 10.0 kV. Dielectric properties of PI composite films were measured using a broadband dielectric/impedance spectrometer (Novocontrol ALPHa-ANB, Germany) in the frequency range of 10^{-2} to 10^{7} Hz. Specimens for dielectric test were prepared with the structure of silver paste/PI film/silver paste.

3. Results and discussion

3.1. Characterization of GiFO and GFO-ODA

FT-IR measurement is conducted to characterize the chemical structures of GiFO and GiFO-ODA after the oxidation and modification processes. Their FT-IR spectra are presented in Fig. 1. The characteristic absorption bands at 1217 cm^{-1} and at 1080 cm^{-1} of GiF are attributed to the stretching vibration of covalent C–F bonds and semi-ionic C–F bonds, respectively.[35,36] Its absorption band at 1630 cm^{-1} related to the stretching vibration of C=C bonds is due to the presence of graphitic phase in commercial unsaturated GiF.[33,37–39] FT-IR spectrum of GiFO shows characteristic absorption bands at 1726 cm^{-1} (C=O stretching vibration), 1348 cm^{-1} (C–O stretching vibration), and 1053 cm^{-1} (C–O–C stretching vibration).[40,41] The stretching vibration of O–H bonds in the region of 3190–3660 cm^{-1} is from the hydroxyl groups, carboxyl groups of GiFO, and the residual water trapped between nanosheets. The band at 1630 cm^{-1} of GiFO becomes weaker because of the smaller graphitic domains in GiFO. After the modification of GFO with ODA, the spectrum of GFO-ODA presents additional peaks at 3376 and 3323 cm^{-1}, which are ascribed to the symmetric and asymmetric stretching vibration of N–H in aromatic amine. The modification of GFO is the nucleophilic attack by amine on the epoxy groups, and hence the absorption band of C–O–C stretching vibration reduced after modification. Moreover, the stretching vibration of phenyl framework at 1499 cm^{-1} also implies that ODA units are grafted onto GFO nanosheets.[42]

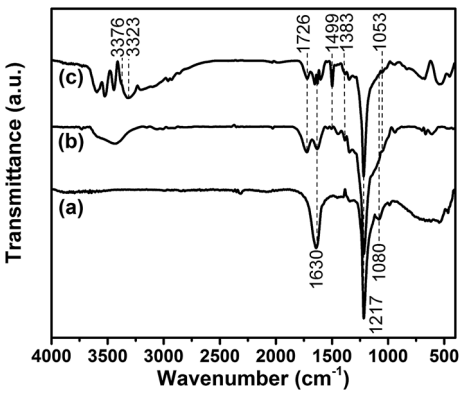

Fig. 1 FT-IR spectra of GiF (a), GiFO (b), and GFO-ODA (c).

XPS spectra of GFO and GFO-ODA are given in Fig. 2. In Fig. 2(a) for C 1s spectrum of GiFO, some typical peaks for oxygen-containing groups, such as C=O (287.1 eV) and C–O (286.1 eV), can be observed, suggesting that GiF have been oxidized to GiFO. The C 1s spectrum of GFO-ODA in Fig. 2(b) shows a significant decrease in C–O content, and the peak for C–N (284.9 eV) confirms that ODA units are covalently attached to GFO nanosheets. This can be further verified by the peaks at 399.6 eV (–NH_2 in amino groups) and 401.3 eV (C–N groups) in the N 1s spectrum of GFO-ODA in Fig. 2(c). Therefore, the result from XPS spectra coincides with the one of FT-IR, indicating the ODA units are successfully incorporated to the GFO nanosheets. The fluorination degree of GiF and GFO-ODA are also characterized by XPS. The fluorine content of GFO-ODA is 16.29%, slightly lower than 20.62% of GiF.

The structural differences between GiF, GiFO, and GFO-ODA were investigated by XRD (Fig. 3). There are the peaks centered at around 13.9° for all three samples, corresponding to an interlayer spacing of 0.64 nm. These peaks are related to the C–F bonds, suggesting the transformation of the sp^2 bonding in grapheme to the sp^3 bonding in GiF, GiFO, and GFO-ODA.[43] The narrow and sharp peak (002) at 26.6° in the XRD pattern of GiF indicates that the nanosheets possess graphitic domains. For GiFO, the presence of the broad peak at ~10.6° and the absence of the peak at ~26.6° suggest that the oxygen-containing functional groups are bonded to GiFO nanosheets and the interlayer spacing is thereby broadened to 0.83 nm.[29,33] Because of the intercalation of ODA into GiFO layers, the interlayer distance of GFO-ODA nanosheets is enlarged to 0.98 nm. According to these results, one can conclude that ODA units have successfully been bonded to the nanosheets.

Fig. 4 illustrates the Raman spectra of GiF and its derivatives. For all samples, there are two strong Raman peaks. The G-bands at ~1575 cm^{-1} correspond to the E_{2g} vibrational mode of C–C with sp^2 hybridization localized inside the planar sheets of graphite, and the D-band at ~1320 cm^{-1} is attributed to the A_{1g} mode in the disordered edge region of the nanosheets.[38] Hence, the ratio between the intensities of D-band and G-band (I_D/I_G) characterizes the number of defects in nanosheets. The values

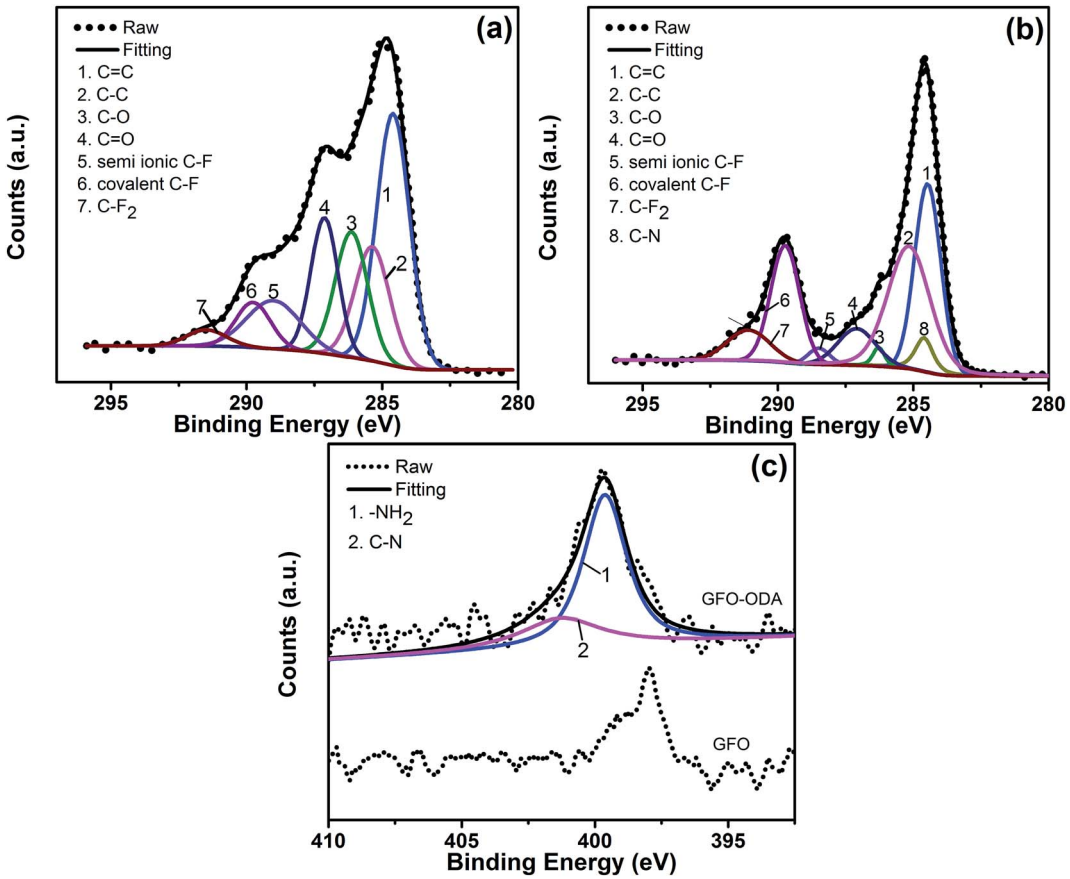

Fig. 2 High resolution C 1s XPS spectra of GiFO (a) and GFO-ODA (b); N 1s XPS spectrum of GiFO and GFO-ODA (c).

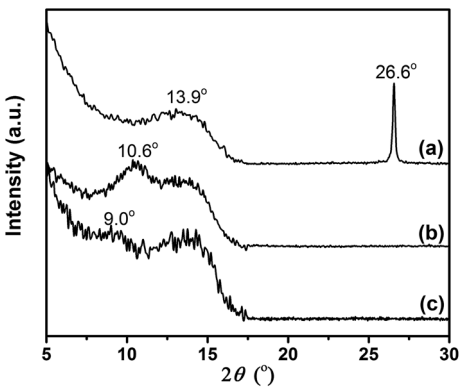

Fig. 3 X-ray diffraction patterns of GiF (a), GiFO (b), and GFO-ODA (c).

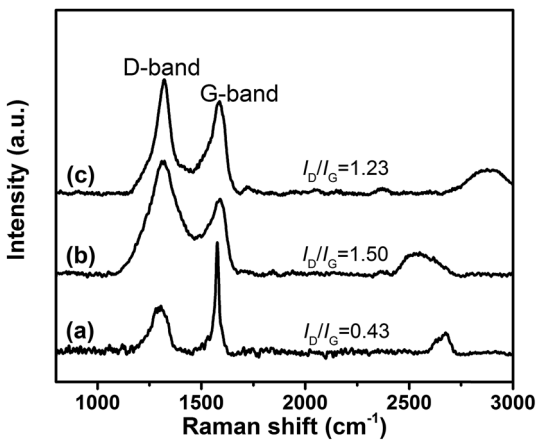

Fig. 4 Raman spectra of GiF (a), GiFO (b), and GFO-ODA (c).

of I_D/I_G increases from 0.43 for GiF to 1.50 for GiFO due to the defects introduced by oxidation. Compared with GiFO, a slightly reduced value of I_D/I_G is obtained for GFO-ODA, indicating that nearly no more defects were introduced in GFO-ODA and partial reduction occurred simultaneously during the modification.

TGA is employed to examine the thermal stability of the prepared GFO-ODA. In Fig. 5, TGA curve of GiF shows a weight loss beginning at 400 °C, which is related to the detachment of fluorine atoms and the decomposition of the carbon skeleton.[43,44] For the as-prepared GiFO, the weight loss happens below 150 °C due to the removal of residual water trapped in the lamellar structure.[45,46] On the contrary, the curve of GFO-ODA shows almost no weight loss below 100 °C due to the partial reduction during modification, which leads less water trapped in GFO-ODA. With the temperature increasing, the TGA curves of GiFO and GFO-ODA show another two major weight loss stages. In the temperature range of 150–300 °C, both of GiFO and GFO-ODA suffer weight loss due to the decomposition of

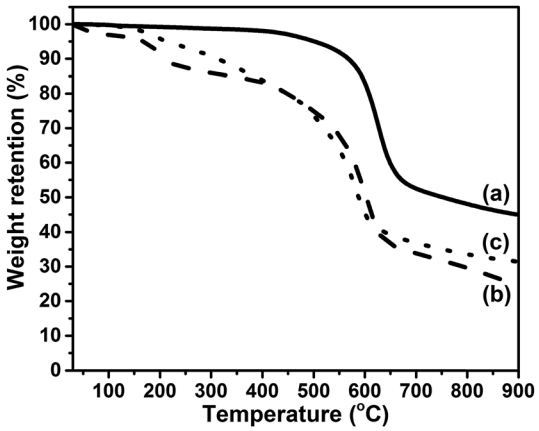

Fig. 5 TGA curves of GiF (a), GiFO (b), and GFO-ODA (c).

the thermally unstable oxygen-containing functional groups, such as hydroxyl and epoxy groups.[17,40] Then a more significant weight loss occurs from 300 to 700 °C, in which the removal of relatively more stable oxygen-containing functional groups takes place and the char is expected to become the sp^2-hybridized carbon.[40,46,47] Differing from GiFO, GFO-ODA decomposes at a more rapid rate in the range of 300–450 °C, which may be ascribed to the thermal degradation of ODA units in addition to the oxygen-containing functional groups. It is worth noting that the char yield of GFO-ODA (~32 wt%) is larger than that of GiFO (~25 wt%). The difference in char yield may be due to the partially reduction of GiFO while being modified,[46,47] consistent with the results obtained above.

3.2. PI morphology

The SEM images of the fractured surfaces of PI films after tensile testing are presented in Fig. 6. The morphology can be used to evaluate the dispersion and compatibility of fillers in PI matrix. The pure PI film possesses a rather smooth and flat fractured surface (Fig. 6(a)). The slightly bright dots and lines indicate that PI film is stretched out upon mechanical deformation. For the GF/PI film, the GF nanosheets aggregated in the PI matrix (arrow in Fig. 6(b)) due to the relatively low surface energy derived from the presence of fluorine atoms. In contrast, the fractured surface of GFO/PI film shows a layered structure, indicating the relatively good dispersion in the PI matrix. Compared with the pure PI film, GFO-ODA/PI film with 1.0 wt% loading has a rougher fractured surface, which can be ascribed to the strong interfacial interactions and the good compatibility between GFO-ODA and PI matrix. As a result, the stress can be transferred from the matrix to the nanosheets. When the content of fillers reaches a critical value, the aggregates of nanosheets tend to form. As the loading of GFO-ODA is increased to 2.0 wt%, some of nanosheets are pulled out during deformation, generating micron-scale holes in the PI matrix (Fig. 6(f)).

3.3. Dielectric properties of films

Complex dielectric constant (ε^*) can be expressed as $\varepsilon^* = \varepsilon' - i\varepsilon''$, where ε' is the real part and ε'' is the imaginary part,

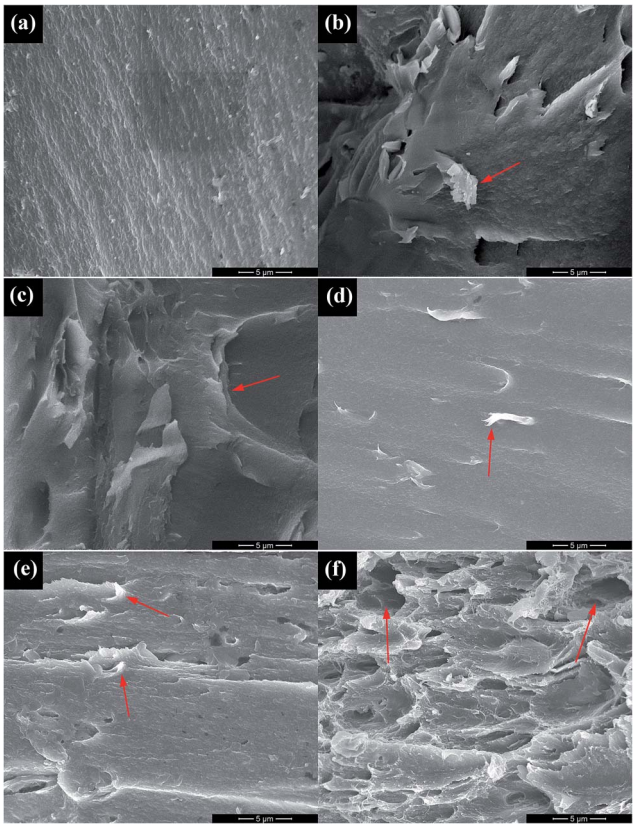

Fig. 6 SEM images of (a) pure PI film, (b) GF/PI film, (c) GFO/PI film, and GFO-ODA/PI films at various loadings: (d) 0.5 wt%, (e) 1.0 wt%, and (f) 2.0 wt%.

respectively. ε' is a measure of the energy stored in the dielectrics through polarization, whereas the loss tangent $\tan\delta$ measures the amount of energy dissipated during molecular motion in the presence of the alternating electric field.

The dependence of the dielectric constants on frequency at room temperature is shown in Fig. 7(a). Under an alternating electric field, the polarization occurs and the dipoles cannot keep up with the variation of the electric field, which results in the decrease of ε' with the increase of frequency. The dielectric constants at 10^6 Hz of pure PI film and PI composite films are summarized in Table 1. Here ε' of pure PI film and PI composite films at 10^6 Hz are selected for comparison because the frequency range from 10^1 to 10^6 Hz is very important for practical applications in microelectronics.[48] GFO-ODA adsorbs and interacts with PI chains. Consequently, GFO-ODA hinders the motion of dipolar moieties and restricts the relaxation of dipoles of PI. It is interesting to see that the dielectric constant of GFO-ODA/PI films does not monotonously decrease with the loading of GFO-ODA. The dielectric constant first decreases with the loading of GFO-ODA until it reaches the minimum value of 2.75 at the loading of 1.0 wt%. However, the dielectric constant of the film with 2.0 wt% GFO-ODA abnormally increases to 4.05, even larger than that of pure PI film. As discussed above, GFO-ODA nanosheets at high contents may aggregate. In the process of preparing GFO-ODA/PAA solutions, the aggregation of GFO-ODA makes it hard for PAA chains to

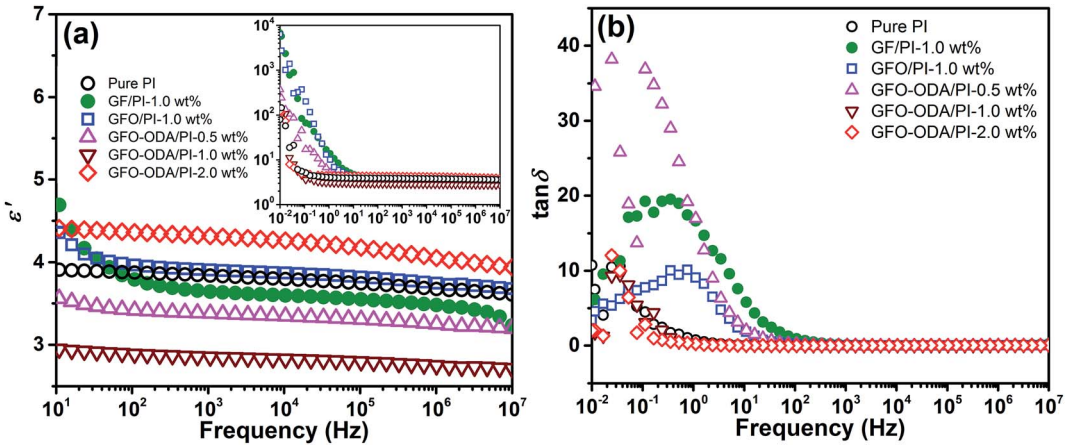

Fig. 7 Dependence of dielectric constant (a) and loss tangent (b) on the frequency for pure PI and PI composites. The inset shows the frequency dependence of dielectric constants in the range from 10^{-2} to 10^{7} Hz.

Table 1 Dielectric properties of pure PI and PI composite films

Samples	Content of filler (wt%)	ε' (10^6 Hz)
Pure PI	—	3.68
GF/PI	1.0	3.48
GFO/PI	1.0	3.75
GFO-ODA/PI	0.5	3.25
GFO-ODA/PI	1.0	2.75
GFO-ODA/PI	2.0	4.05

intercalate with GFO-ODA, promoting the microphase separation and less effective restriction on the PI chains. In addition, the interface between the aggregate and PI matrix generates an interfacial polarization. Consequently, both effects lead to a high dielectric constant for 2.0 wt% GFO-ODA/PI. For comparison, the dielectric properties of GF/PI and GFO/PI films are also studied. The introduction of GF into PI resin reduces the dielectric constant of GF/PI film to 3.48, which was slightly lower than that of pure PI film. The decrease in the dielectric constant has its origin in high electronegativity of the fluorine atoms and the low polarizability of the C–F bond, as well as the lowered water absorption. For GFO/PI film, however, its dielectric constant increased to 3.75, mainly due to the hydrophilic nature of oxygen-containing functional groups. In Fig. 7(b), the loss tangent peaks of GF/PI and GFO/PI films shift to the higher frequencies compared with pure PI, indicating the weakened interactions between PI chains. In contrast, the loss peak of GFO-ODA/PI film with 1.0 wt% loading shifts to lower frequencies compared with GFO/PI film, which suggests the modification of GFO with ODA can effectively improve the interaction between nanosheets and PI matrix.

Slightly larger values of dielectric constants of GFO-ODA/PI in the lower frequency range may be originated from one or more polarizations, such as interfacial polarization or Maxwell–Wagner–Sillars effect, electrode polarization, and conductivity phenomena.[49] It is more effective to employ electric modulus formalism rather than dielectric constant formalism to analyze the information given in the dielectric spectroscopy, since the large variation in dielectric constants and loss factors at low frequencies can be minimized in electric modulus formalism.[49–51] By using electric modulus formalism, some problems in the analysis of dielectric relaxation in the dielectric constant formalism, such as the contact of electrode/specimen, the space charges injection phenomena, or absorbed impurity, can be solved or even neglected. The complex electric modulus (M^*) is defined as the inverse of the complex dielectric constant,

$$M^* = \frac{1}{\varepsilon^*} = \frac{\varepsilon'}{\varepsilon'^2 + \varepsilon''^2} + \mathrm{i}\frac{\varepsilon''}{\varepsilon'^2 + \varepsilon''^2} = M' + \mathrm{i}M'' \qquad (1)$$

where M' and M'' are the real and imaginary part of electric modulus, respectively. The dependence of the real part of electric modulus (M') on frequency is plotted in Fig. 8(a). From low to high frequencies, the curves of all specimens pass through a transition, which implies the relaxation processes. In Fig. 8(b), the curves of the imaginary part as a function of frequency possess loss peaks in the transition region. These peaks are related to the glass transition of PI matrix. Compared to pure PI, the loss peak of GF/PI film shifts to higher frequencies, which is considered as an indication for the weakened interactions between PI chains. The incorporation of GF loosens the stacking of PI chains, increases free volume, and facilitates the motion of segments. For GFO/PI film, however, the oxygen-containing groups and more absorbed water increase its dielectric constant. On the contrary, the loss peak of GFO-ODA/PI with 1.0 wt% loading shifts to lower frequencies compared with pure PI film, which indicates that the incorporation of GFO-ODA restricts the motion of PI chains *via* covalent bonding between the nanosheets and PI matrix. Such bonds hinder the orientation of the dipolar moieties and thereby reduce the dielectric constant. Moreover, a few loss peaks can be observed in low frequencies for 2.0 wt% of GFO-ODA. This phenomenon is a result of interfacial polarization or Maxwell–Wagner–Sillars effect, which usually occurs in electrically heterogeneous systems derived from the accumulation of mobile charges at the interface. In the present case, the

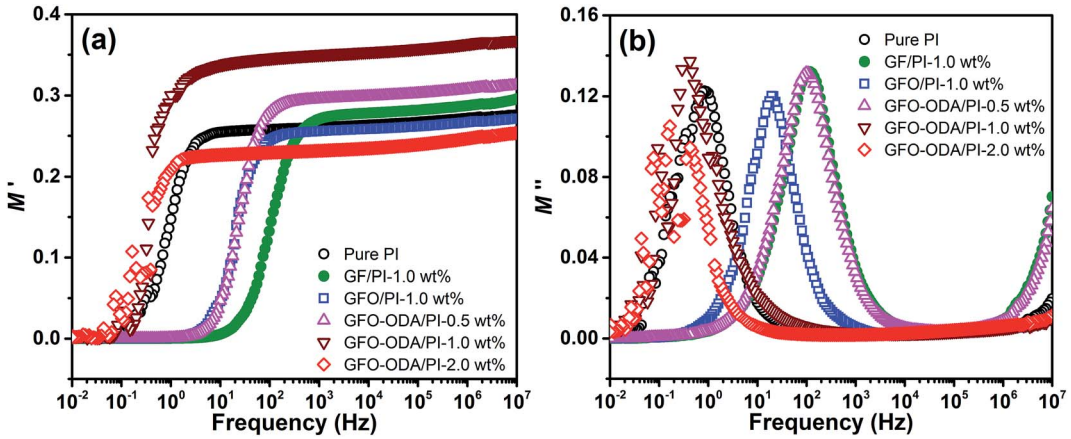

Fig. 8 Real (a) and imaginary (b) parts of electric modulus *vs.* frequency for pure PI and PI composite.

aggregation of GFO-ODA increases dielectric constant, which is in agreement with the explanation proposed above.

3.4. Tensile tests

The effect of GFO-ODA loading on the mechanical properties of PI composite films is summarized in Table 2. GFO-ODA nanosheets with amino groups can provide reactive sites for the polymerization of PAA and strongly interact with PI matrix. Furthermore, GFO-ODA nanosheets may act as the cross-linking agent to restrict the chains movement, which improves the mechanical properties of GFO-ODA/PI films. As expected, with 1.0 wt% GFO-ODA loading, Young's modulus and tensile strength of GFO-OFA/PI film are significantly increased to 3.89 GPa and 110 MPa from 2.82 GPa and 97.0 MPa for pure PI, respectively. The reinforcement can be attributed to the good dispersion of GFO-ODA nanosheets in PI matrix. Since the nanosheets strongly interact with PI chains *via* covalent bonding, the load can be efficiently transferred from the matrix to the strong nanosheets and hence improves the mechanical properties of GFO-ODA/PI films. Simultaneously, the elongation at break declines to only 10.9%, indicating that the film becomes less flexible. As the GFO-ODA loading increases to 2.0 wt%, both of Young's modulus and the tensile strength do not change significantly.

The mechanical properties of GF/PI and GFO/PI films are also measured. Young's modulus of the former is ~20% greater than that of pure PI film, while the elongation at break hardly changes due to the weak interaction between GF and the PI matrix. Besides, the low surface energy of GF makes it difficult to be dispersed well so that the contact area between GF and PI matrix is too small to transfer stress efficiently. The elongation at break for the GFO/PI film, however, is decreased to 30.0%. The reason

Table 2 Mechanical properties of pure PI and PI composite films

Samples	Content of filler (wt%)	Young's modulus (GPa)	Tensile strength (MPa)	Elongation at break (%)
Pure PI	—	2.82 ± 0.03	97.0 ± 1.8	47.0 ± 0.7
GF/PI	1.0	3.44 ± 0.11	101 ± 4.0	43.1 ± 3.6
GFO/PI	1.0	3.79 ± 0.10	107 ± 2.1	30.0 ± 2.6
GFO-ODA/PI	0.5	3.54 ± 0.21	105 ± 5.3	23.9 ± 2.8
GFO-ODA/PI	1.0	3.89 ± 0.08	110 ± 1.3	10.9 ± 2.7
GFO-ODA/PI	2.0	3.88 ± 0.09	107 ± 3.9	11.5 ± 1.9

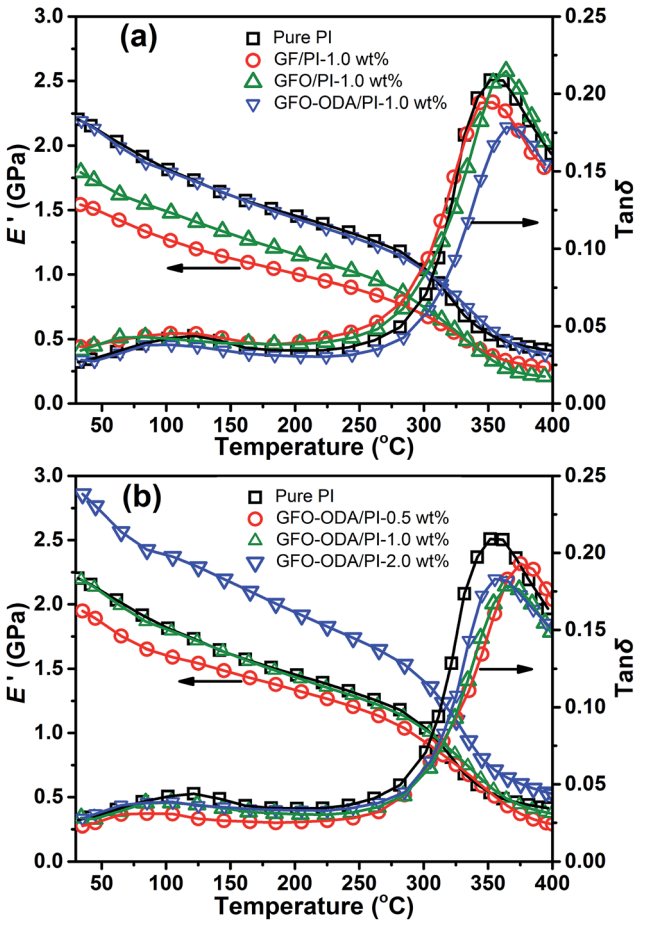

Fig. 9 Storage modulus and tan δ in DMA of (a) PI composite films with various fillers and (b) GFO-ODA/PI films at different contents.

Table 3 Dynamic mechanical and thermal properties of pure PI and PI composite films

		DMA		TGA	
Samples	Content of filler (wt%)	E'^{a} (GPa)	$T_g{}^{b}$ (°C)	$T_{5d}{}^{c}$ (°C)	Char yield^{d} (wt%)
Pure PI	—	2.20	356	572	59.5
GF/PI	1.0	1.55	348	588	59.6
GFO/PI	1.0	1.81	361	574	57.5
GFO-ODA/PI	0.5	1.99	359	582	58.1
GFO-ODA/PI	1.0	2.21	366	582	58.0
GFO-ODA/PI	2.0	2.86	360	572	57.5

[a] Determined by DMA at about 30 °C. [b] Determined by DMA at maximum of tan δ. [c] The temperature of weight loss at 5 wt% determined by TGA. [d] Determined by TGA at 900 °C.

may be that GFO nanosheets act as the physical cross-linking agents *via* the hydrogen bonds between the oxygen-containing functional groups on GFO nanosheets and the polar groups in PI chains. The incorporation of GFO restricts the movement of the PI chains and makes the GFO/PI film brittle.

Both Young's modulus and tensile strength of GFO/PI film are smaller than those of GFO-ODA/PI film at the same content of GFO. The good dispersion of nanosheets within the PI matrix and the strong interaction between the fillers and matrix are responsible for the improved mechanical properties of PI composite films.

3.5. Dynamic mechanical properties

The storage modulus (E') and loss tangent (tan δ) are characterized by DMA (Fig. 9), and the data are listed in Table 3. Among PI composite films with different fillers at 1 wt% content, GFO-ODA/PI film possesses the maximum value of E', whereas GF/PI film has the minimum value. Such behaviors are due to the different strengths of interaction between the nanosheets and PI matrix as discussed above. The glass transition temperatures (T_g) of these composite films follows the order of E'. GFO-ODA/PI film possesses the maximum increase of T_g because of the effective restriction of PI chains.

For GFO-ODA/PI films at temperatures below T_g, the value of E' increases when the loading increases from 0.5 wt% to 2.0 wt%. The T_g of these films, however, does not monotonously shift to the higher temperature with the increase of GFO-ODA loading. The maximum value occurs at the content of 1.0 wt%. Combined with the analysis of dielectric properties, one can conclude that there are two opposite influences of the incorporation of GFO-ODA nanosheet on PI matrix. One is to loosen the stacking of PI chains, and the other is to restrict the motion of PI chains. Hence, in the case of 0.5 wt% loading, T_g is almost the same as that of pure PI film. When the loading increases to 2.0 wt%, the aggregation of the excess GFO-ODA nanosheets may be mainly responsible for the reduction of T_g, which is in an agreement with the above testing results.

3.6. Thermal stability

Thermal stability is one of the important properties of PI films since they are often used as dielectrics in microelectronics where the annealing step at the temperature up to 400 °C is often necessary.[2] TGA results of the pure PI film and the PI composite films are listed in Table 3. The thermal stability of PI films can usually be improved by the incorporation of inorganic fillers. The temperature at 5 wt% weight loss (T_{5d}) changes from 572 °C for pure PI film to 582 °C for 1.0 wt% GFO-ODA/PI. If uniformly dispersed, modified graphene can improve the thermal properties of PI by blocking heat transfer and decreasing volatilization of degradation products. However, at 2.0 wt% loading, modified graphene is poorly dispersed and aggregates, and hence it cannot improve the thermal stability. Moreover, introduction of GFO-ODA into the system makes the amino groups more than anhydride groups, which affects the molecular weight of PI. For GFO/PI and GFO-ODA/PI films, their thermal stability does not become worse than that of the pure PI film. Thus the incorporation of GFO-ODA into PI matrix is a facile method to fabricate high performance PI nanocomposite films.

4. Conclusions

In this study, we proposed an effective approach to fabricate the novel fluorine-containing PI nanocomposite films with low dielectric constant. The obtained GFO-ODA nanosheets, as a reactive platform for covalently bonding with PI chains, provided large contact area and strong interfacial interactions with PI matrix. The dielectric constant of the GFO-ODA/PI films showed a non-monotonic change while the loading increased. The minimum value of 2.75 (at 10^6 Hz) was achieved at 1.0 wt% loading. Furthermore, the GFO-ODA/PI films maintained the excellent mechanical and thermal properties. Young's modulus of the GFO-ODA/PI film with 1.0 wt% loading was 50% greater than that of the pure PI film. Besides, the incorporation of GFO-ODA did not decrease T_g and decomposition temperature of the pure PI film. GFO-ODA/PI film is a potential material with low dielectric constant for a wide range of applications.

Acknowledgements

This research is supported by the National Natural Science Foundation of China (No. 51173047, 51573054) and the Project for Science and Technology of Guangdong Province (2014B090916001).

Notes and references

1 D. J. Liaw, K. L. Wang, Y. C. Huang, K. R. Lee, J. Y. Lai and C. S. Ha, *Prog. Polym. Sci.*, 2012, **37**, 907–974.
2 G. Maier, *Prog. Polym. Sci.*, 2001, **26**, 3–65.
3 W. Volksen, R. D. Miller and G. Dubois, *Chem. Rev.*, 2009, **110**, 56–110.
4 M. Hasegawa and K. Horie, *Prog. Polym. Sci.*, 2001, **26**, 259–335.
5 L. Tao, H. Yang, J. Liu, L. Fan and S. Yang, *Polymer*, 2009, **50**, 6009–6018.
6 W. Jang, D. Shin, S. Choi, S. Park and H. Han, *Polymer*, 2007, **48**, 2130–2143.
7 M. G. Dhara and S. Banerjee, *Prog. Polym. Sci.*, 2010, **35**, 1022–1077.
8 K. S. Novoselov, A. K. Geim, S. V. Morozov, D. Jiang, Y. Zhang, S. V. Dubonos, I. V. Grigorieva and A. A. Firsov, *Science*, 2004, **306**, 666–669.
9 C. Lee, X. Wei, J. W. Kysar and J. Hone, *Science*, 2008, **321**, 385–388.
10 A. A. Balandin, S. Ghosh, W. Bao, I. Calizo, D. Teweldebrhan, F. Miao and C. N. Lau, *Nano Lett.*, 2008, **8**, 902–907.
11 M. Orlita, C. Faugeras, P. Plochocka, P. Neugebauer, G. Martinez, D. K. Maude, A.-L. Barra, M. Sprinkle, C. Berger, W. A. de Heer and M. Potemski, *Phys. Rev. Lett.*, 2008, **101**, 267601.
12 J. S. Bunch, S. S. Verbridge, J. S. Alden, A. M. van der Zande, J. M. Parpia, H. G. Craighead and P. L. McEuen, *Nano Lett.*, 2008, **8**, 2458–2462.
13 R. Sengupta, M. Bhattacharya, S. Bandyopadhyay and A. K. Bhowmick, *Prog. Polym. Sci.*, 2011, **36**, 638–670.
14 H. Kim, A. A. Abdala and C. W. Macosko, *Macromolecules*, 2010, **43**, 6515–6530.
15 D. Cai and M. Song, *J. Mater. Chem.*, 2010, **20**, 7906–7915.
16 D. R. Dreyer, S. Park, C. W. Bielawski and R. S. Ruoff, *Chem. Soc. Rev.*, 2010, **39**, 228–240.
17 S. Stankovich, D. A. Dikin, R. D. Piner, K. A. Kohlhaas, A. Kleinhammes, Y. Jia, Y. Wu, S. T. Nguyen and R. S. Ruoff, *Carbon*, 2007, **45**, 1558–1565.
18 J. Kim, L. J. Cote and J. Huang, *Acc. Chem. Res.*, 2012, **45**, 1356–1364.
19 J. I. Paredes, S. Villar-Rodil, A. Martínez-Alonso and J. M. D. Tascón, *Langmuir*, 2008, **24**, 10560–10564.
20 M. J. McAllister, J. L. Li, D. H. Adamson, H. C. Schniepp, A. A. Abdala, J. Liu, M. Herrera-Alonso, D. L. Milius, R. Car, R. K. Prud'homme and I. A. Aksay, *Chem. Mater.*, 2007, **19**, 4396–4404.
21 R. R. Nair, W. Ren, R. Jalil, I. Riaz, V. G. Kravets, L. Britnell, P. Blake, F. Schedin, A. S. Mayorov, S. Yuan, M. I. Katsnelson, H. M. Cheng, W. Strupinski, L. G. Bulusheva, A. V. Okotrub, I. V. Grigorieva, A. N. Grigorenko, K. S. Novoselov and A. K. Geim, *Small*, 2010, **6**, 2877–2884.
22 J. T. Robinson, J. S. Burgess, C. E. Junkermeier, S. C. Badescu, T. L. Reinecke, F. K. Perkins, M. K. Zalalutdniov, J. W. Baldwin, J. C. Culbertson, P. E. Sheehan and E. S. Snow, *Nano Lett.*, 2010, **10**, 3001–3005.
23 K. J. Jeon, Z. Lee, E. Pollak, L. Moreschini, A. Bostwick, C. M. Park, R. Mendelsberg, V. Radmilovic, R. Kostecki, T. J. Richardson and E. Rotenberg, *ACS Nano*, 2011, **5**, 1042–1046.
24 C. Sun, Y. Feng, Y. Li, C. Qin, Q. Zhang and W. Feng, *Nanoscale*, 2014, **6**, 2634–2641.
25 A. Tuteja, W. Choi, M. Ma, J. M. Mabry, S. A. Mazzella, G. C. Rutledge, G. H. McKinley and R. E. Cohen, *Science*, 2007, **318**, 1618–1622.
26 W. Huang, Q. X. Pei, Z. Liu and Y. W. Zhang, *Chem. Phys. Lett.*, 2012, **552**, 97–101.
27 Z. Wang, J. Wang, Z. Li, P. W. Gong, J. F. Ren, H. G. Wang, X. X. Han and S. R. Yang, *RSC Adv.*, 2012, **2**, 11681–11686.
28 K. I. Ho, C. H. Huang, J. H. Liao, W. Zhang, L. J. Li, C. S. Lai and C. Y. Su, *Sci. Rep.*, 2014, **4**, 5893.
29 A. B. Bourlinos, A. Bakandritsos, N. Liaros, S. Couris, K. Safarova, M. Otyepka and R. Zbořil, *Chem. Phys. Lett.*, 2012, **543**, 101–105.
30 A. Mathkar, T. N. Narayanan, L. B. Alemany, P. Cox, P. Nguyen, G. H. Gao, P. Chang, R. Romero-Aburto, S. A. Mani and P. M. Ajayan, *Part. Part. Syst. Charact.*, 2013, **30**, 266–272.
31 D. Damien, P. M. Sudeep, T. N. Narayanan, M. R. Anantharaman, P. M. Ajayan and M. M. Shaijumon, *RSC Adv.*, 2013, **3**, 25702–25706.
32 R. Romero-Aburto, T. N. Narayanan, Y. Nagaoka, T. Hasumura, T. M. Mitcham, T. Fukuda, P. J. Cox, R. R. Bouchard, T. Maekawa, D. S. Kumar, S. V. Torti, S. A. Mani and P. M. Ajayan, *Adv. Mater.*, 2013, **25**, 5632–5637.
33 S. J. Yan, J. Q. Zhao, Y. C. Yuan, S. M. Liu, Z. X. Huang, Z. G. Chen, D. Jiang and W. X. Zhao, *RSC Adv.*, 2013, **3**, 21869–21876.
34 W. S. Hummers Jr and R. E. Offeman, *J. Am. Chem. Soc.*, 1958, **80**, 1339.
35 X. Wang, Y. Dai, J. Gao, J. Huang, B. Li, C. Fan, J. Yang and X. Liu, *ACS Appl. Mater. Interfaces*, 2013, **5**, 8294–8299.
36 Y. S. Lee, T. H. Cho, B. K. Lee, J. S. Rho, K. H. An and Y. H. Lee, *J. Fluorine Chem.*, 2003, **120**, 99–104.
37 M. Dubois, J. Giraudet, K. Guérin, A. Hamwi, Z. Fawal, P. Pirotte and F. Masin, *J. Phys. Chem. B*, 2006, **110**, 11800–11808.
38 V. Gupta, T. Nakajima and B. Žemva, *J. Fluorine Chem.*, 2001, **110**, 145–151.
39 S. S. Han, T. H. Yu, B. V. Merinov, A. C. T. van Duin, R. Yazami and W. A. Goddard III, *Chem. Mater.*, 2010, **22**, 2142–2154.
40 D. C. Marcano, D. V. Kosynkin, J. M. Berlin, A. Sinitskii, Z. Sun, A. Slesarev, L. B. Alemany, W. Lu and J. M. Tour, *ACS Nano*, 2010, **4**, 4806–4814.
41 X. Zhang, Y. Feng, D. Huang, Y. Li and W. Feng, *Carbon*, 2010, **48**, 3236–3241.
42 J. Dong, C. Yin, X. Zhao, Y. Z. Li and Q. H. Zhang, *Polymer*, 2013, **54**, 6415–6424.

43 Y. Liu, R. L. Vander Wal and V. N. Khabashesku, *Chem. Mater.*, 2007, **19**, 778–786.
44 R. Zbořil, F. Karlický, A. B. Bourlinos, T. A. Steriotis, A. K. Stubos, V. Georgakilas, K. Šafářová, D. Jančík, C. Trapalis and M. Otyepka, *Small*, 2010, **6**, 2885–2891.
45 Z. Xu and C. Gao, *Macromolecules*, 2010, **43**, 6716–6723.
46 B. Zhang, Y. Chen, X. Zhuang, G. Liu, B. Yu, E.-T. Kang, J. Zhu and Y. Li, *J. Polym. Sci., Part A: Polym. Chem.*, 2010, **48**, 2642–2649.
47 J. F. Shen, Y. Z. Hu, M. Shi, X. Lu, C. Qin, C. Li and M. X. Ye, *Chem. Mater.*, 2009, **21**, 3514–3520.
48 Z. M. Dang, L. J. Ma, J. W. Zha, S. H. Yao, D. Xie, Q. Chen and X. Duan, *J. Appl. Phys.*, 2009, **105**, 44104.
49 K. G. Gatos, J. G. M. Alcázar, G. C. Psarras, R. Thomann and J. Karger-Kocsis, *Compos. Sci. Technol.*, 2007, **67**, 157–167.
50 G. M. Tsangaris, G. C. Psarras and N. Kouloumbi, *J. Mater. Sci.*, 1998, **33**, 2027–2037.
51 G. C. Psarras, K. G. Gatos, P. K. Karahaliou, S. N. Georga, C. A. Krontiras and J. Karger-Kocsis, *eXPRESS Polym. Lett.*, 2007, **1**, 837–845.